

# Denoising Hyperspectral Image with Non-i.i.d. Noise Structure

Yang Chen, Xiangyong Cao, Qian Zhao, Deyu Meng, *Member, IEEE*, Zongben Xu

**Abstract**—Hyperspectral image (HSI) denoising has been attracting much research attention in remote sensing area due to its importance in improving the HSI qualities. The existing HSI denoising methods mainly focus on specific spectral and spatial prior knowledge in HSIs, and share a common underlying assumption that the embedded noise in HSI is independent and identically distributed (i.i.d.). In real scenarios, however, the noise existed in a natural HSI is always with much more complicated non-i.i.d. statistical structures and the under-estimation to this noise complexity often tends to evidently degenerate the robustness of current methods. To alleviate this issue, this paper attempts the first effort to model the HSI noise using a non-i.i.d. mixture of Gaussians (NMoG) noise assumption, which is finely in accordance with the noise characteristics possessed by a natural HSI and thus is capable of adapting various noise shapes encountered in real applications. Then we integrate such noise modeling strategy into the low-rank matrix factorization (LRMF) model and propose a NMoG-LRMF model in the Bayesian framework. A variational Bayes algorithm is designed to infer the posterior of the proposed model. All involved parameters can be recursively updated in closed-form. Compared with the current techniques, the proposed method performs more robust beyond the state-of-the-arts, as substantiated by our experiments implemented on synthetic and real noisy HSIs.

**Index Terms**—Hyperspectral image denoising, Non-i.i.d. Noise modeling, Low-rank matrix factorization.

## I. INTRODUCTION

**H**YPERSPECTRAL image (HSI) is captured from sensors over various bands and contains abundant spatial and spectral knowledge across all these bands beyond the traditional gray-scale or RGB images. Due to its preservation of full-bands information under a real scene, it has been widely used in military and civilian aspects such as terrain detection, mineral exploration, pharmaceutical counterfeiting, vegetation and environmental monitoring [10], [16], [40], [42], [52], [56]. In real cases, however, a HSI is always corrupted by noises due to equipment limitations, such as sensor sensitivity, photon effects and calibration error [45]. Besides, due to the limited radiance energy and generally narrow band width, the energy captured by each sensor might be low and thus the shot noise and thermal noise then always happen inevitably. These noise severely degrades the quality of the imagery and limits the performance of the subsequent processing, i.e., classification [43], unmixing [2], [41] and target detection [46], on data. Therefore, it is a critical preprocessing step to reduce the HSI noise [20], [39] to a general HSI processing task.

Yang Chen, Xiangyong Cao, Qian Zhao, Deyu Meng (corresponding author), Zongben Xu are with the School of Mathematics and Statistics and Ministry of Education Key Lab of Intelligent Networks and Network Security, Xi'an Jiaotong University, Xi'an 710049, China (e-mail: dymeng@mail.xjtu.edu.cn).

The simplest denoising way is to utilize the traditional 2-D or 1-D denoising methods to reduce noise in the HSI pixel by pixel [17] or band by band [12], [14], [30], [44], [50]. However, this kind of processing method ignores the correlations between different spectral bands or adjacent pixels, and often results in a relatively low-quality result. Recently, more efficient methods have been proposed to handle this issue. The main idea is to elaborately encode the prior knowledge on the structure underlying a natural HSI, especially the characteristic across the spatial and spectral dimensionality. E.g., Othman and Qian [38] made an initial attempt to this issue by designing a hybrid spatial-spectral derivative-domain wavelet shrinkage model based on the dissimilarity of the signal regularity existing along the space and spectrum of a natural HSI. And then Chen et al. [5] proposed another approach to encoding both spatial and spectral knowledge by combining the bivariate wavelet thresholding with principal component analysis. To further enhance the denoising capability, Yuan et al. [51] employed a spectral-spatial adaptive total variation. Later, Chen et al. [9] proposed a spatially adaptive weighted prior by combining the smoothness and discontinuity preserving properties along the spectral domain. By further considering the spatial and spectral dependencies, Zhong and Wang [58] proposed a multiple-spectral-band CRF (MSB-CRF) model in a unified probabilistic framework.

Besides, by explicitly treating HSI data as a tensor, a series of methods that expanding wavelet-based method from 2-D to 3-D has been proposed. E.g., Dabov [11] designed VBM3D method by applying the concepts of grouping and collaborative filtering to video denoising. Then, Letexier et al. [28] proposed a generalized multi-dimensional Wiener filter for denoising hyperspectral image. Similarly, Chen et al. [6] extended Sendur and Selesnick's bivariate wavelet thresholding from 2-D image denoising to 3-D data cube denoising. For better denoising results, Chen et al. [7] proposed a new signal denoising algorithm by using neighbouring wavelet coefficients, which considered both translation-invariant (TI) and non-TI versions. Later, as an extension of BM3D method, Maggioni et al. [32] presented BM4D model. Meanwhile, another type of method that based on tensor decomposition has appeared. Karami et al. [26] developed a Genetic Kernel Tucker Decomposition (GKTD) algorithm to exploit both spectral and the spatial information in HSIs. To address the uniqueness of multiple ranks of Tucker Decomposition, Liu et al. [31] proposed PARAFAC method that make the number of estimated rank reduced to one. Later, Peng et al. [39] proposed a decomposable nonlocal tensor dictionary learning (TDL) model, which fully considered the non-local similarity

over space and the global correlation across spectrum. Among these methods, BM4D and TDL achieved the state-of-the-art performance in more general noisy MSI cases.

Most of current HSI denoising methods have mainly considered the HSI prior spectral and spatial knowledge into their methods, while only use  $L_2$  loss term to rectify the deviation between the reconstruction and the original HSI. In the viewpoint of statistical theory, the utilization of such loss term implies that the HSI data noise follows an i.i.d. Gaussian distribution. However, in real scenarios, HSI noises generally have more complicated statistical structures. This means that such easy loss term is too subjective to reflect the real cases and inclines to degenerate the performance of the methods in more complex while more realistic non-i.i.d. noise case .

The idea of considering more complex HSI noise beyond only Gaussian in HSI denoising has been attracting attention very recently in the framework of low-rank matrix analysis. Since adjacent HSI bands usually exhibit strong correlations, by reshaping each band as a vector and stacking all the vectors into a matrix, the reshaped HSI matrix can be assumed to be with low rank. Various low-rank matrix models have been presented in different noise scenes in recent decades. Along this line, the classical Low-rank Matrix Factorization (LRMF) model is presented by K.Mitra et al. [37] and T.Okatani et al. [36] for Gaussian noise, and its global optimal solution can be directly obtained by using Singular Value Decomposition (SVD) [18]. To add more robustness, the  $L_1$ -norm LRMF [13], [15], [25], [27] is generally used and many algorithms have been designed to solve this model, such as  $L_1$  Wiberg [15], CWM [35] and RegL1ALM [57]. This  $L_1$ -norm LRMF model actually assumes an i.i.d. Laplacian noises embedded in data. To handle more complex noise cases, Meng and De la Torre [34] modeled the noise as more adaptable i.i.d. mixture of Gaussians (MoG) distributions to represent noise. Such noise modeling idea was further extended to the Bayesian framework by Chen et al. [8], to RPCA by Zhao et al. [55] and to the tensor factorization by Chen et al. [49]. Very recently, Cao et al. [?], [4] modeled the noise as a more general i.i.d. mixture of Exponential Power (MoEP) distribution, which achieves competitive performance in HSI denoising under real noise scenarios. Besides, some other attempts have also been proposed to model the noise as a combination of sparse and Gaussian noise [1], and Zhang et al. [54] also utilized this idea for HSI denoising task. Later, He et al. [21] further enhance the capability of the method by adding a TV regularization to low-rank reconstruction. Besides, based on the mixture noise assumption, He et.al [19] proposed a noise-adjusted low-rank methods and Wang et al. [47] proposed a GLRR denoising method for the reconstruction of the corrupted HSIs. All these approaches also achieve good performance on HSI denoising in mixed noise cases.

From Gaussian noise assumption to MoEP noise assumption, such advancements make the model more adaptive to various HSI noises encountered in practice. However, all of the aforementioned LRMF models just simply assume that the HSI noise is i.i.d., which is more or less deviated from the practical scenarios, where the noises in a HSI is generally with non-i.i.d. configurations. In this sense, there is still a large room

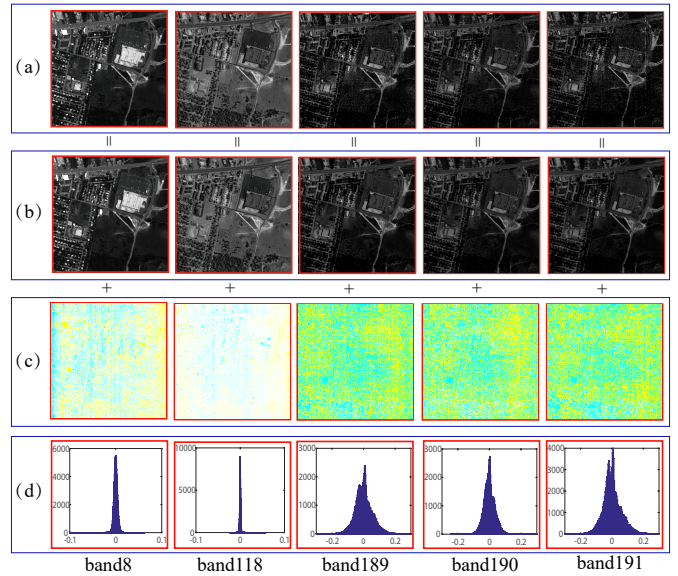


Fig. 1. (a) Different bands of images in the original HSI. (b) Restored HSIs obtained by our proposed method. (c) Extracted noise by the proposed method. (d) Histograms of the noise in all bands.

to further improve the capability of current HSI denoising techniques especially under real complicated scenarios.

To make this point clearer, let's try to analyze some evident noise characteristics possessed by a HSI collected from real cases. Fig. 1 presents a real HSI case for auxiliary understanding. Firstly, an image in a band is generally collected under the similar sensor setting, and thus the i.i.d. distribution is a rational assumption for the noise over the elements in the band. This can be evidently observed from the band-noise of the HSI image shown in Fig. 1. Secondly, due to the difference of the sensor sensitivity for collecting images located in various HSI bands, the noise of different-band-images always depicts evident distinctions [19]. From Fig. 1, it is easy to see that images located in some bands are very clean, while are extremely noisy in some others [16], [53]. Thirdly, albeit different, the noise distributions along different bands have certain correlation. E.g., along adjacent bands, the noise tends to be more or less similar since images on neighboring spectrums are generally collected under small deviation of sensor settings and wavelength [58]. From Fig. 1, it is easy to see the noise similarity for images located in 189-191 bands. Accordingly, the real HSI noise distribution is generally non-i.i.d. and has a more complicated configurations than the i.i.d. noise assumption of the current HSI denoising techniques. Such deviation inclines to make their performance degenerate under more practical cases, which will be clearly observed in our experiments.

To address this issue, this paper proposes a new noise modeling framework, by carefully designing noise distribution structure to make it possibly faithfully deliver the real HSI noise configurations. Specifically, we model the noise of each HSI band with different Mixture of Gaussian (MoG) distributions (i.e., parameters of MoG are different). Besides, MoG parameters across different bands are encoded under a similar top-level prior distribution, representing the correlation

between noise distributions across different bands. In this way, the non-i.i.d. noise structure under a practical HSI image can be more properly encoded and an appropriate HSI denoising effect is thus to be expected.

In this study, we embed such noise modeling framework into the low-rank matrix factorization (LRMF) realization, which easily assumes a low-rank structure (both spatial and spectral) of the to-be-recovered HSI. Our experimental results show that, even under this simple setting of HSI structure, such noise modeling idea can greatly help enhance the HSI denoising ability beyond previous techniques and obtain the state-of-the-art performance in real HSI denoising tasks.

The rest of the paper is organized as follows: The proposed model and the corresponding variational inference algorithm are presented in Section 2. Experimental results are shown in Section 3. Finally, conclusions are drawn in Section 4. Throughout the paper, we denote scalars, vectors, matrices, tensors as non-bold letters, bold lower case letters, bold upper case letters and decorated letters, respectively.

## II. NON-I.I.D. MOG METHOD FOR HSI DENOISING

In this section, we first introduce our non-i.i.d. noise encoding strategy and then propose a non-i.i.d. MoG LRMF (NMoG-LRMF) model by using this strategy in the LRMF model for HSI denoising. Finally, the corresponding variational inference algorithm for the proposed model is designed.

### A. Non-i.i.d. noise encoding

Let's represent a given HSI as a matrix  $\mathbf{Y} \in \mathbb{R}^{N \times B}$ , where  $N$  and  $B$  mean the spatial and spectral dimensions of the HSI, respectively. By assuming that noise is additive, we have the following expression:

$$\mathbf{Y} = \mathbf{L} + \mathbf{E}, \quad (1)$$

where  $\mathbf{L} \in \mathbb{R}^{N \times B}$  denotes the clean HSI and  $\mathbf{E} \in \mathbb{R}^{N \times B}$  denotes the embedded noise.

In the previous section, we have summarized three intrinsic properties possessed by HSI noise: (i) Noise of an image located in the same band are i.i.d.; (ii) Noise of images located in different bands are non-identical; (iii) Noise distributions in different bands are correlated.

Based on the above properties (i) and (ii) of HSI noise structure, we model noise located in each band as an independent MoG distribution while assume that the parameters for MoG distributions in different bands are different. The MoG is utilized due to its universal approximation capability for any continuous densities [33], which has been extensively used and studied in [34], [55].

Denote  $e_{ij}$  as the element located in  $i^{th}$  row and  $j^{th}$  column of the noise matrix  $\mathbf{E}$ , and as aforementioned, the noise distribution located in the  $j^{th}$  band can then be modeled as:

$$p(e_{ij}) = \sum_{k=1}^K \pi_{jk} \mathcal{N}(e_{ij} | \mu_{jk}, \tau_{jk}^{-1}), \quad (2)$$

where  $\pi_{jk}$  is the mixing proportion with  $\pi_{jk} \geq 0$  and  $\sum_{k=1}^K \pi_{jk} = 1$ ,  $K$  is the Gaussian component number,  $\mu_{jk}$  and

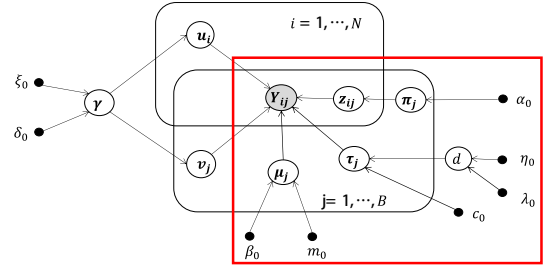


Fig. 2. Graphical model of NMoG-LRMF.  $Y_{ij}$  denotes the  $i^{th}$  HSI element in its  $j^{th}$  band.  $\mathbf{u}_i$  and  $\mathbf{v}_j$  are columns of low-rank matrix  $\mathbf{U}$  and  $\mathbf{V}$ , respectively, generated from a Gaussian distribution with precise  $\gamma$ , with Gamma prior distribution with hyper-parameters  $\xi_0$  and  $\delta_0$ . The portion in the red box corresponds to the noise encoding part.  $\mu_{jk}$ ,  $\tau_{jk}$  are the  $k$ -dimensional vectors representing the mean and variance of all MoG components in the  $j^{th}$  band, with hyper-parameters  $\beta_0, m_0, d, c_0$ , where  $d$  is with hyper-parameters  $\eta_0, \lambda_0$ .  $z_{ij}$  is the hidden variable generated from Multinomial distribution with parameter  $\pi_j$ , with hyper-parameters  $\alpha_0$ .

$\tau_{jk}$  are mean and precision of the  $k^{th}$  Gaussian component in the  $j^{th}$  band, respectively. Note that MoG parameters  $\pi_{jk}, \mu_{jk}$  and  $\tau_{jk}$  are different, implying different MoG distributions across different bands.

Considering the noise property (iii), we further provide the hypothesis that MoG parameters  $\mu_{jk}$ s and  $\tau_{jk}$ s of all bands are generated from a two-level prior distribution:

$$\begin{aligned} \mu_{jk}, \tau_{jk} &\sim \mathcal{N}(\mu_{jk} | m_0, (\beta_0 \tau_{jk})^{-1}) \text{Gam}(\tau_{jk} | c_0, d), \\ d &\sim \text{Gam}(d | \eta_0, \lambda_0), \end{aligned} \quad (3)$$

where  $\text{Gam}(\cdot)$  represents the Gamma distribution. In this way, the correlation between noise distributions among different bands is then rationally encoded. Through introducing a latent variable  $z_{ijk}$ , we can equivalently rewrite Eq. (2) as the following form:

$$\begin{aligned} e_{ij} &\sim \prod_{k=1}^K \mathcal{N}(e_{ij} | \mu_{jk}, \tau_{jk}^{-1})^{z_{ijk}}, \\ z_{ij} &\sim \text{Multinomial}(z_{ij} | \pi_j), \\ \pi_j &\sim \text{Dir}(\pi_j | \alpha_0), \end{aligned} \quad (4)$$

where  $\text{Multinomial}(\cdot)$  and  $\text{Dir}(\cdot)$  represent the Multinomial and Dirichlet distributions, respectively. Then, Eq. (3) and (4) together encode the noise structure embedded in a HSI. Fig. 2 shows the graphical model for noise encoding within the red box. All involved parameters can be inferred from data, as introduced in the following Section II.C.

### B. NMoG-LRMF model

For the prior structure of the underlying clean HSI matrix  $\mathbf{L}$ , we readily employ the low-rank structure to encode it. Specifically, let's consider the following LRMF model:

$$\mathbf{Y} = \mathbf{U}\mathbf{V}^T + \mathbf{E}, \quad (5)$$

where  $\mathbf{L} = \mathbf{U}\mathbf{V}^T$  implies the low-rank structure underlying the clean HSI.

For most deterministic LRMF model, the rank  $r$  of matrix  $\mathbf{L}$  is fixed. By modeling the problem into certain generative model [1], [55], the rank can also be adaptively learned from

data. Specifically, suppose the columns of  $\mathbf{U}$  and  $\mathbf{V}$  are generated from Gaussian distribution. For  $l = 1, 2, \dots, R$ , where  $R$  is a preset larger value beyond the true rank  $r$ , then

$$\mathbf{u}_{\cdot l} \sim \mathcal{N}(\mathbf{u}_{\cdot l} | 0, \gamma_l^{-1} \mathbf{I}_N), \quad \mathbf{v}_{\cdot l} \sim \mathcal{N}(\mathbf{v}_{\cdot l} | 0, \gamma_l^{-1} \mathbf{I}_B), \quad (6)$$

where  $\mathbf{u}_{\cdot l}$  and  $\mathbf{v}_{\cdot l}$  are the  $l^{\text{th}}$  columns of  $\mathbf{U}$  and  $\mathbf{V}$ , respectively.  $\mathbf{I}_N (\mathbf{I}_B)$  denotes the  $N \times N (B \times B)$  identity matrix.  $\gamma_l$  is the precision of  $\mathbf{u}_{\cdot l}$  and  $\mathbf{v}_{\cdot l}$  with prior as follows:

$$\gamma_l \sim \text{Gam}(\gamma_l | \xi_0, \delta_0). \quad (7)$$

Note that each column pair  $\mathbf{u}_{\cdot l}$  and  $\mathbf{v}_{\cdot l}$  of  $\mathbf{U}$ ,  $\mathbf{V}$  has the same sparsity profile characterized by the common precision variable  $\gamma_l$ . It has been validated that such a modeling could lead to large precision values of some  $\gamma_l$ s, and hence is capable of automatically conducting low-rank estimate of  $\mathbf{L}$  [1].

Combining Eqs. (2)-(7) together, we can construct the full NMoG-LRMF Bayesian model. And the graphical model representation of this model is shown in Fig. 2. The goal turns to infer the posterior of all involved variables:

$$p(\mathbf{U}, \mathbf{V}, \mathcal{Z}, \boldsymbol{\mu}, \boldsymbol{\tau}, \boldsymbol{\pi}, \boldsymbol{\gamma}, d | \mathbf{Y}), \quad (8)$$

where  $\mathcal{Z} = \{z_{ij}\}_{N \times B}$ ,  $\boldsymbol{\mu} = \{\mu_{jk}\}_{B \times K}$ ,  $\boldsymbol{\tau} = \{\tau_{jk}\}_{B \times K}$ ,  $\boldsymbol{\pi} = (\boldsymbol{\pi}_1, \dots, \boldsymbol{\pi}_B)$ ,  $\boldsymbol{\gamma} = (\gamma_1, \dots, \gamma_R)$ .

### C. Variational Inference

We use variational Bayes (VB) method [3] to infer the posterior. Specifically, VB aims to use a variational distribution  $q(\boldsymbol{\theta})$  to approximate the true posterior  $p(\boldsymbol{\theta} | \mathbf{D})$ , where  $\boldsymbol{\theta}$  denotes the set of parameters and  $\mathbf{D}$  denotes the observed data. To achieve this goal, we need to solve the following optimization problem:

$$\min_{q \in \mathbb{C}} KL(q(\boldsymbol{\theta}) || p(\boldsymbol{\theta} | \mathbf{D})) = - \int q(\boldsymbol{\theta}) \ln \left\{ \frac{p(\boldsymbol{\theta} | \mathbf{D})}{q(\boldsymbol{\theta})} \right\} d\boldsymbol{\theta}, \quad (9)$$

where  $KL(q || p)$  represents the KL divergence between two distribution  $q$  and  $p$ , and  $\mathbb{C}$  denotes the constraint set of probability densities to make the minimization tractable. Assuming  $\mathbb{C}$  is the distribution family which can be factorized with respect to some disjoint groups:  $q(\boldsymbol{\theta}) = \prod_i q_i(\boldsymbol{\theta}_i)$ , the closed-form optimal solution  $q_i^*(\boldsymbol{\theta}_i)$  can be obtained by

$$q_i^*(\boldsymbol{\theta}_i) = \frac{\exp\{\langle \ln p(\boldsymbol{\theta}, \mathbf{D}) \rangle_{\boldsymbol{\theta} \setminus \boldsymbol{\theta}_i}\}}{\int \exp\{\langle \ln p(\boldsymbol{\theta}, \mathbf{D}) \rangle_{\boldsymbol{\theta} \setminus \boldsymbol{\theta}_i}\}}, \quad (10)$$

where  $\langle \cdot \rangle$  denotes the expectation and  $\boldsymbol{\theta} \setminus \boldsymbol{\theta}_i$  denotes the set of  $\boldsymbol{\theta}$  with  $\boldsymbol{\theta}_i$  removed.

Then we can analytically infer all the factorized distributions involved in Eq. (8). Suppose that the approximation of posterior distribution (8) possesses a factorized form as follows:

$$q(\mathbf{U}, \mathbf{V}, \mathcal{Z}, \boldsymbol{\mu}, \boldsymbol{\tau}, \boldsymbol{\pi}, \boldsymbol{\gamma}, d) = \prod_i q(\mathbf{u}_{\cdot i}) \prod_j q(\mathbf{v}_{\cdot j}) \prod_{ij} q(z_{ij}) \prod_j q(\boldsymbol{\mu}_j, \boldsymbol{\tau}_j) q(\boldsymbol{\pi}_j) \prod_l q(\gamma_l) q(d), \quad (11)$$

where  $\mathbf{u}_{\cdot i}$  ( $\mathbf{v}_{\cdot j}$ ) are the  $i^{\text{th}}$  ( $j^{\text{th}}$ ) row of matrix  $\mathbf{U}$  ( $\mathbf{V}$ ), respectively. According to Eq. (10), we can get the closed-

form inference equation for each component of (11)<sup>1</sup>.

**Estimation of noise component:** We first list the updating equation for the noise components involved in Eq. (11). The posterior distribution of mean and precision for noise in each band is updated by the following equation:

$$q^*(\boldsymbol{\mu}_j, \boldsymbol{\tau}_j) = \prod_k \mathcal{N}(\mu_{jk} | m_{jk}, \frac{1}{\beta_{jk} \tau_{jk}}) \text{Gam}(\tau_{jk} | c_{jk}, d_{jk}), \quad (12)$$

where the parameters in the above equation can be calculated from data in the following way:

$$m_{jk} = \frac{1}{\beta_{jk}} \{ \beta_0 m_0 \sum_i \langle z_{ijk} \rangle (Y_{ij} - \langle \mu_{jk} \rangle) \}, \quad (13)$$

$$\beta_{jk} = \beta_0 + \sum_i \langle z_{ijk} \rangle, \quad c_{jk} = c_0 + \frac{1}{2} \sum_i \langle z_{ijk} \rangle, \quad (14)$$

$$d_{jk} = \langle d \rangle + \frac{1}{2} \left\{ \sum_i \langle z_{ijk} \rangle \langle (Y_{ij} - \mathbf{u}_i \mathbf{v}_j^T)^2 \rangle + \beta_0 m_0^2 - \frac{1}{\beta_{jk}} \left[ \sum_i \langle z_{ijk} \rangle (Y_{ij} - \mathbf{u}_i \mathbf{v}_j^T) + \beta_0 m_0^2 \right]^2 \right\}. \quad (15)$$

The update equation of the latent variable  $\mathcal{Z}$  is:

$$q^*(z_{ij}) = \prod_k \varrho_{ijk}^{z_{ijk}}, \quad (16)$$

where the involved parameters are calculated by

$$\begin{aligned} \varrho_{ijk} &= \rho_{ijk} / \sum_k \rho_{ijk}, \\ \ln \rho_{ijk} &= \langle \ln \pi_{jk} \rangle - \ln \sqrt{2\pi} + \langle \ln \tau_{jk} \rangle / 2 \\ &\quad - \langle \tau_{jk} (Y_{ij} - \mu_{jk} - \mathbf{u}_i \mathbf{v}_j^T)^2 \rangle / 2. \end{aligned} \quad (17)$$

Similarly, the update equation for the mixing proportion  $\boldsymbol{\pi}_j$  over the  $j^{\text{th}}$  band can be written as:

$$q^*(\boldsymbol{\pi}_j) = \prod_k \pi_{jk}^{\alpha_{jk} - 1}, \quad (18)$$

where  $\alpha_{jk} = \alpha_{0k} + \sum_i \langle z_{ijk} \rangle$ .

The update equation on the hyper-parameter  $d$  is:

$$q^*(d) = \text{Gam}(d | \eta, \lambda), \quad (19)$$

where  $\eta = \eta_0 + c_0 KB$  and  $\lambda = \lambda_0 + \sum_{j,k} \langle \tau_{jk} \rangle$ .

**Estimation of low-rank component.** Completing the component update for noise, we then estimate the posterior of low-rank component  $\mathbf{u}_i$  ( $i = 1, \dots, N$ ) and  $\mathbf{v}_j$  ( $j = 1, \dots, B$ ) as:

$$q^*(\mathbf{u}_{\cdot i}) = \mathcal{N}(\mathbf{u}_{\cdot i} | \boldsymbol{\mu}_{\mathbf{u}_{\cdot i}}, \boldsymbol{\Sigma}_{\mathbf{u}_{\cdot i}}), \quad (20)$$

where

$$\begin{aligned} \boldsymbol{\mu}_{\mathbf{u}_{\cdot i}} &= \left\{ \sum_{j,k} \langle z_{ijk} \rangle \langle \tau_{jk} \rangle (Y_{ij} - \langle \mu_{jk} \rangle) \langle \mathbf{v}_{\cdot j} \rangle \right\} \boldsymbol{\Sigma}_{\mathbf{u}_{\cdot i}}, \\ \boldsymbol{\Sigma}_{\mathbf{u}_{\cdot i}} &= \left\{ \sum_{j,k} \langle z_{ijk} \rangle \langle \tau_{jk} \rangle \langle \mathbf{v}_{\cdot j}^T \mathbf{v}_{\cdot j} \rangle + \langle \boldsymbol{\Gamma} \rangle \right\}^{-1}. \end{aligned}$$

$$q^*(\mathbf{v}_{\cdot j}) = \mathcal{N}(\mathbf{v}_{\cdot j} | \boldsymbol{\mu}_{\mathbf{v}_{\cdot j}}, \boldsymbol{\Sigma}_{\mathbf{v}_{\cdot j}}), \quad (21)$$

where

$$\begin{aligned} \boldsymbol{\mu}_{\mathbf{v}_{\cdot j}} &= \left\{ \sum_{i,k} \langle z_{ijk} \rangle \langle \tau_{jk} \rangle (Y_{ij} - \langle \mu_{jk} \rangle) \langle \mathbf{u}_{\cdot i} \rangle \right\} \boldsymbol{\Sigma}_{\mathbf{v}_{\cdot j}}, \\ \boldsymbol{\Sigma}_{\mathbf{v}_{\cdot j}} &= \left\{ \sum_{i,k} \langle z_{ijk} \rangle \langle \tau_{jk} \rangle \langle \mathbf{u}_{\cdot i}^T \mathbf{u}_{\cdot i} \rangle + \langle \boldsymbol{\Gamma} \rangle \right\}^{-1}, \end{aligned} \quad (22)$$

<sup>1</sup>Inference details to obtain these equations can be referred to in <http://dymeng.gr.xjtu.edu.cn>.

where  $\mathbf{\Gamma} = \text{diag}(\langle \gamma \rangle)$ . For  $\gamma_l$  which controls the rank of  $\mathbf{U}$  and  $\mathbf{V}$ , we have :

$$q^*(\gamma_l) = \text{Gam}(\gamma_r | \xi_l, \delta_l), \quad (23)$$

where

$$\begin{aligned} \xi_l &= \xi_0 + (m + n)/2, \\ \delta_l &= \delta_0 + \sum_i \langle u_{il}^2 \rangle / 2 + \sum_j \langle v_{jl}^2 \rangle / 2. \end{aligned}$$

$m$  and  $n$  represent the image size among the spatial dimension. As discussed by Babacan et al. [1], some  $\gamma_l$ s tend to be very large during the inference process and the corresponding rows will be removed from  $\mathbf{U}$  and  $\mathbf{V}$ . The low-rank purpose can thus be rationally conducted. In all our experiments, we just automatically infer the rank of the reconstructed matrix through throwing away those comparatively very large  $\gamma_l$  as previous literatures did [55].

The proposed variational inference method for the NMoG-LRMF model can then be summarized in Algorithm 1.

---

**Algorithm 1** NMoG-LRMF algorithm

---

**Input:** the original HSI matrix  $\mathbf{Y} \in \mathbb{R}^{N \times B}$ , Gaussian component number  $K$ , and maximum iteration number.

**Output:**  $\mathbf{U}_{\text{opt}} = \mathbf{U}_t$ ,  $\mathbf{V}_{\text{opt}} = \mathbf{V}_t$ .

**Initialization:** Parameters  $(m_0, \beta_0, c_0, d_0, \eta_0, \lambda_0)$  in noise prior. Low-rank components  $\mathbf{U}_0, \mathbf{V}_0$  and parameters in model prior  $(\xi_0, \delta_0)$ ;  $t = 1$ .

- 1: **while** not covered **do**
  - 2:   Update approximate posterior of noise component  $\mathcal{Z}^t, \boldsymbol{\pi}^t$  by Eq. (16)-(18).
  - 3:   Update approximate posterior of noise component  $\boldsymbol{\mu}^t, \boldsymbol{\tau}^t$  by Eq. (12)-(15).
  - 4:   Update approximate posterior of noise component  $d^t$  by Eq. (19).
  - 5:   Update approximate posterior of low-rank component  $\mathbf{U}^t, \mathbf{V}^t$  by Eq. (20)-(22).
  - 6:   Update approximate posterior of parameters in noise component  $\boldsymbol{\gamma}^t$  by Eq. (23).
  - 7:    $t \leftarrow t + 1$ .
  - 8: **end while**
- 

**Setting of hyper-parameters:** We set all the hyper-parameters involved in our model in a non-informative manner to make them possibly less affect the inference of posterior distributions [3]. Throughout our experiments, we set  $m_0$  as 0, and  $\beta_0, c_0, d_0, \eta_0, \lambda_0, \xi_0, \delta_0$  as a small value  $10^{-3}$ . Our method performs stably well under such easy settings.

### III. EXPERIMENTAL RESULTS

In this section, to evaluate the performance of the proposed NMoG-LRMF method, we conducted a series of experiments on both synthetic and real HSI data. Compared methods include LRMR [54] and LRTV [21], considering deterministic Gaussian noise and sparse noise. Meanwhile, five representative low-rank matrix analysis methods considering different kinds of i.i.d. noise distributions were also considered for comparison, including PMoEP [4] (assuming i.i.d. mixture of Exponential Power noise), MoG-RPCA [55] (assuming i.i.d. MoG noise), RegL1ALM [57], CWM [35] (assuming i.i.d. Laplace noise) and SVD [18] (assuming i.i.d. Gaussian noise).

Besides, the performance of TDL [39] and BM4D [32] are also compared, and both methods represent the state-of-the-art methods for HSI denoising by considering HSI priors. All experiments were implemented in Matlab R2014b on a PC with 4.0GHz CPU and 31.4GB RAM.

#### A. Simulated HSI denoising experiments

In this experiment, we focus on the performance of NMoG-LRMF in HSI denoising with synthetic noise. Two HSIs were employed: Washington DC Mall<sup>2</sup> with size of  $1208 \times 307 \times 191$  and RemoteImage<sup>3</sup> provided by Liu et. al. [29] with size of  $205 \times 246 \times 96$ . After cropping the main part of HSI and deleting some evident visual contaminative spectral channels, Washington DC Mall and RemoteImage are resized to  $200 \times 200 \times 160$  and  $200 \times 200 \times 89$ , respectively. The gray value of each band are normalized into  $[0, 1]$ .

Real-world HSIs are usually contaminated by several different types of noise, including the most common Gaussian noise, impulse noise, dead pixels or lines, and stripes [54]. In order to simulate these real HSI noise scenarios, we added six kinds of noises to the original HSI data.

(1) *I.i.d. Gaussian noise:* Entries in all bands were corrupted by zero-mean i.i.d. Gaussian noise  $N(0, \sigma^2)$  with  $\sigma = 0.05$ .

(2) *Non-i.i.d. Gaussian noise:* Entries in all bands were corrupted by zero-mean Gaussian noise with different intensity. The signal noise ratio (SNR) value of each band is generated from uniform distribution with value in the range of  $[5, 10]$  dB.

(3) *Gaussian + Stripe noise:* All bands were corrupted by Gaussian noise as Case (2). Besides, 40 bands in DCmall data (30 bands in RemoteImage data) were randomly chosen to add stripe noise. The number of stripes in each band is from 20 to 40.

(4) *Gaussian + Deadline noise:* Each band was contaminated by Gaussian noise as Case (2). 40 bands in DCmall data (30 bands in RemoteImage data) were chosen randomly to add deadline noise. The number of deadline is from 5 to 15.

(5) *Gaussian + Impluse noise:* All bands were corrupted by Gaussian noise as Case (2). 40 bands in DCmall (30 bands in RemoteImage data) were randomly chosen to added impluse noise with different intensity, and the percentage of impluse is from 50% to 70%.

(6) *Mixture noise:* Each band was randomly corrupted by at least one kind of noise mentioned in case (2)-(5).

Three criteria were utilized to measure performance: (1) MPSNR [24]: Mean of peak signal-to-noise ratio (PSNR) over all bands between clean HSI and recovered HSI. (2) MSSIM [48]: Mean of structural similarity (SSIM) between clean HSI and recovered HSI over all bands. (3) Time: Time cost of each method used to complete the denoising process.

The parameters of competing methods are set as follows: the block size in LRMR is  $20 \times 20 \times B$  and the step size is 10. For LRTV,  $\epsilon_1 = \epsilon_2 = 10^{-8}$  and  $\lambda = 1/\sqrt{NB}$ . For TDLd, we set the block size as  $6 \times 6 \times B$  and the step size is 2. For BM4D, we set the block size as  $8 \times 8 \times 8$  and

<sup>2</sup><http://engineering.purdue.edu/~biehl/MultiSpec/hyperspectral.html>

<sup>3</sup>[http://peterwonka.net/Publications/code/LRTC\\_Package\\_Ji.zip](http://peterwonka.net/Publications/code/LRTC_Package_Ji.zip)

TABLE I  
PERFORMANCE COMPARISON OF ALL COMPETING METHODS ON DCMALL DATA WITH SYNTHETIC NOISE.

	Noisy HSI	SVD	RegL1ALM	CWM	MoG-RPCA	PMoEP	LRMR	LRTV	TDL	BM4D	NMoG
i.i.d. Gaussian Noise											
MPSNR	26.02	44.76	41.19	42.89	45.26	44.26	42.48	43.83	<b>46.08</b>	39.33	45.27
MSSIM	0.513	0.983	0.965	0.973	0.985	0.980	0.972	0.977	<b>0.989</b>	0.948	0.985
time	-	<b>0.290</b>	221.2	851.1	59.1	201.7	5367.0	512.3	44.9	965.2	77.8
Non i.i.d. Gaussian Noise											
MPSNR	40.96	43.34	47.15	45.00	46.15	44.09	48.26	47.19	41.80	45.50	<b>51.11</b>
MSSIM	0.890	0.973	0.985	0.980	0.981	0.973	0.987	0.986	0.903	0.983	<b>0.990</b>
time	-	<b>0.292</b>	212.0	800.2	121.5	1672.3	778.6	478.9	821.2	940.8	106.7
Gaussian + Stripe Noise											
MPSNR	44.72	46.14	48.89	48.74	48.54	48.08	51.11	49.06	44.94	46.66	<b>54.16</b>
MSSIM	0.941	0.989	0.992	0.992	0.992	0.990	0.994	0.993	0.942	0.985	<b>0.997</b>
time	-	<b>0.515</b>	238.5	782.6	307.6	1505.5	414.4	683.2	843.1	369.5	334.7
Gaussian + Deadline noise											
MPSNR	44.36	44.08	48.95	47.81	48.65	46.95	50.34	48.95	44.84	46.02	<b>54.04</b>
MSSIM	0.938	0.980	0.993	0.990	0.991	0.986	0.991	0.993	0.943	0.979	<b>0.997</b>
time	-	<b>0.291</b>	177.6	690.4	136.2	2004.7	670.8	321.2	772.3	307.5	143.6
Gaussian + Impluse Noise											
MPSNR	43.05	44.05	49.16	47.51	49.89	46.79	51.05	49.11	43.65	45.77	<b>52.96</b>
MSSIM	0.925	0.981	0.993	0.991	0.993	0.986	0.994	0.993	0.932	0.977	<b>0.997</b>
time	-	<b>0.293</b>	181.3	567.4	146.5	1640.9	743.6	501.3	695.3	1028.6	150.2
Mixture Noise											
MPSNR	42.93	43.32	48.75	44.82	47.94	44.26	48.77	48.54	43.22	43.97	<b>50.38</b>
MSSIM	0.913	0.977	0.991	0.982	0.989	0.978	0.986	0.991	0.917	0.968	<b>0.996</b>
time	-	<b>0.289</b>	176.5	688.7	136.3	940.3	708.2	358.9	653.8	325.4	142.0

TABLE II  
PERFORMANCE COMPARISON OF ALL COMPETING METHODS ON REMOTEIMAGE DATA WITH SYNTHETIC NOISE.

	Noisy HSI	SVD	RegL1ALM	CWM	MoG-RPCA	PMoEP	LRMR	LRTV	TDL	BM4D	NMoG
i.i.d. Gaussian Noise											
MPSNR	26.02	38.19	36.63	36.78	38.66	36.72	37.46	37.89	<b>39.81</b>	38.98	38.65
MSSIM	0.591	0.956	0.937	0.939	0.964	0.956	0.946	0.949	<b>0.971</b>	0.971	0.964
time	-	<b>0.247</b>	105.9	331.6	65.7	38.1	409.1	211.9	47.7	357.7	69.6
Non i.i.d. Gaussian Noise											
MPSNR	25.17	34.36	35.51	35.37	36.41	35.67	35.95	35.73	29.74	36.82	<b>38.26</b>
MSSIM	0.539	0.902	0.921	0.922	0.942	0.928	0.926	0.927	0.729	0.952	<b>0.962</b>
time	-	<b>0.253</b>	105.4	329.3	100.2	301.9	398.7	220.2	151.0	327.8	101.1
Gaussian + Stripe Noise											
MPSNR	29.08	37.48	39.31	38.64	39.70	38.62	40.13	39.36	29.76	37.03	<b>40.68</b>
MSSIM	0.710	0.955	0.968	0.964	0.974	0.965	0.971	0.968	0.731	0.938	<b>0.983</b>
time	-	<b>0.279</b>	108.9	375.8	88.6	299.8	606.4	238.3	1969.9	160.4	112.3
Gaussian + Deadline noise											
MPSNR	27.97	33.37	39.08	37.94	39.58	38.20	38.74	38.72	29.98	34.02	<b>40.43</b>
MSSIM	0.693	0.907	0.967	0.961	0.972	0.963	0.958	0.965	0.772	0.888	<b>0.983</b>
time	-	<b>0.299</b>	108.9	361.7	119.6	1205.9	725.1	378.9	273.5	683.6	127.5
Gaussian + Impluse Noise											
MPSNR	28.20	35.00	41.89	39.48	41.15	39.15	41.32	40.63	30.63	36.97	<b>42.90</b>
MSSIM	0.660	0.917	0.983	0.971	0.981	0.969	0.977	0.977	0.745	0.951	<b>0.990</b>
time	-	<b>0.236</b>	100.0	317.2	110.1	202.8	473.1	251.6	190.7	445.3	118.1
Mixture Noise											
MPSNR	25.84	31.55	37.93	35.72	38.68	36.09	37.76	38.31	26.93	30.29	<b>39.32</b>
MSSIM	0.590	0.868	0.958	0.936	0.966	0.940	0.944	0.962	0.633	0.782	<b>0.979</b>
time	-	<b>0.283</b>	122.0	416.4	69.5	650.7	696.4	260.8	312.2	86.7	105.0

the step size is 4. For NMoG-LRMF method, The component number  $K$  in each band was fixed as 1 in Case (1)-(2), and 3 in Case (3)-(6). The rank of all low-rank based methods is set as 5 in Dcmall data experiment and 4 in RemoteImage data experiment. All parameters involved in the competing methods were empirically tuned or specified as suggested by the related literatures to guarantee their possibly good performance. All competing methods run with 20 random initializations in each noise case, and the average result is reported.

The results of all competing methods in Dcmall and RemoteImage HSI data are shown in Table I and Table II, respectively. The superiority of the proposed method can be easily observed, except in the i.i.d. Gaussian noise case, which complies with the basic noise assumption of conventional

methods. In i.i.d. Gaussian case, instead of only using the simple low-rank prior in our method, multiple competing methods, like TDL and BM4D, utilize more useful HSI priors in their model, and thus tend to have relatively better performance. While on more complex but more practical complicated non-i.i.d. noise cases, the advantage of the proposed method is evident. This can be easily explained by the better noise fitting capability of the proposed method, i.e., it can more properly extract noises embedded in HSI, which then naturally leads to its better HSI recovery performance.

Furthermore, it also can be seen that the computational cost of the proposed method is with almost similar order of magnitude with other competing methods, except the known SVD, which we use the mature toolkit in Matlab and can be

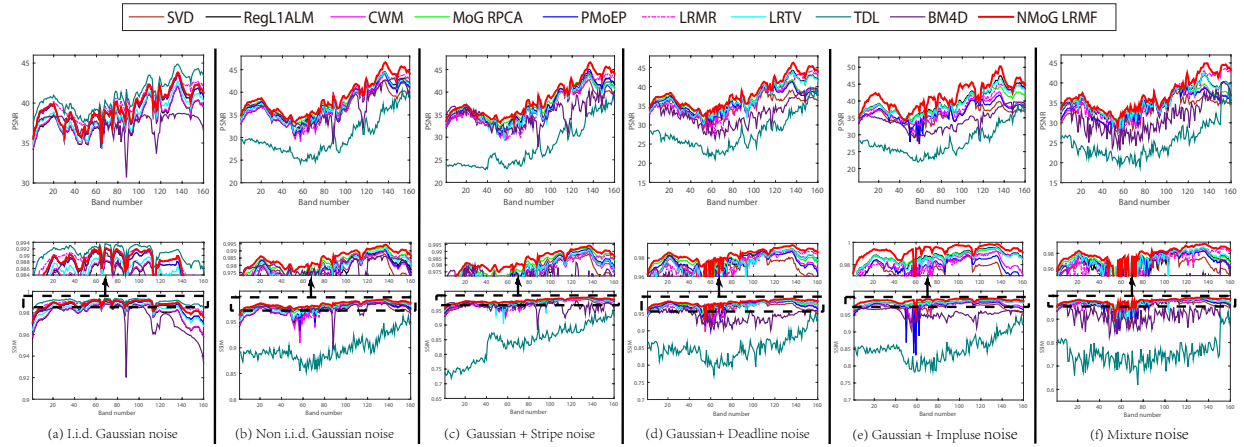


Fig. 3. Each column shows the average PSNR and SSIM measurements among 20 initializations of all methods under certain type of noise in DCmall data: (a) Gaussian noise. (b) Gaussian + Stripe noise. (c) Gaussian + Deadline noise. (d) Gaussian + Impluse noise. (e) Mixture noise. The demarcated area of the subfigure indicates the curve locality on a larger scale.

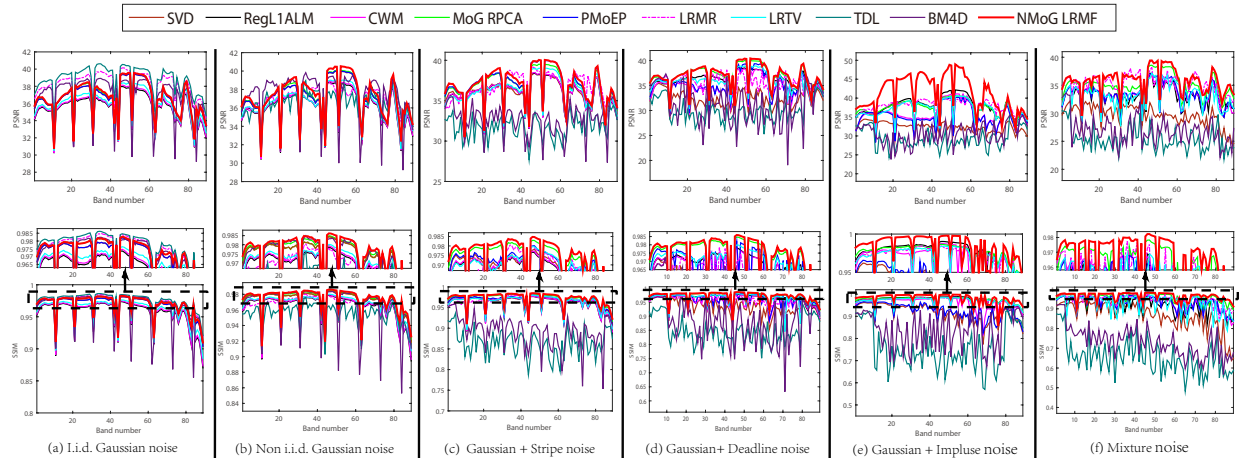


Fig. 4. Each column shows the average PSNR and SSIM measurements among 20 initializations of all methods under certain type of noise in RemoteImage data: (a) Gaussian noise. (b) Gaussian + Stripe noise. (c) Gaussian + Deadline noise. (d) Gaussian + Impluse noise. (e) Mixture noise.

implemented very efficiently. Considering its better capability in fitting much wider range of noises than current methods, it should be rational to say that the proposed method is efficient.

We further show the PSNR and SSIM measurements across all bands of the HSI under six types of noise settings in two experiments in Fig. 3 and Fig. 4, respectively. From the figures, it is easy to see that TDL obtains the best PSNR and SSIM values across all bands in the i.i.d. Gaussian noise. In other more complex noise cases, NMoG-LRMF achieves the best PSNR and SSIM values across almost all bands. This verifies the robustness of the proposed method over entire HSI bands.

Figs. 5 and 6 give the restoration results of two typical bands in DCmall and RemoteImage HSIs, respectively. The original HSIs are corrupted by mixture of Gaussian, stripes, deadline and impluse noise. It can be observed that the competing methods SVD, CWM, PMoEP, LRM, and BM4D can hardly remove this complex mixture noise from the images. We can also see that although RegL1ALM, MoG-RPCA and LRTV have a better denoising performance, the restored HSI still relatively blur many details as compared with the ground truth, which are also reflected from their PSNR and SSIM values in the band. Comparatively, our NMoG-LRMF method achieves

better reconstruction effect both visually and quantitatively, and both finely removes the unexpected noises, and better recovers HSI details like edges and textures.

### B. Real HSI denoising experiments

In this section, we evaluate the performance of the proposed method on two real HSI datasets, Urban dataset<sup>4</sup> and EO-1 Hyperion dataset<sup>5</sup>.

The similar competing methods as the last section were compared in the real HSI experiments. Like the synthetic experiments, all involved parameters have been finely tuned or directly suggested by the original references to promise a possibly well performance of all competing methods. The component number of each band in the proposed method is easily set as 3 throughout all experiments. The gray value of HSI were normalized into [0, 1].

The first Urban dataset is of the size  $307 \times 307 \times 210$ , and some bands are seriously polluted by atmosphere and water. We use all of data without removing any bands to more

<sup>4</sup><http://www.tec.army.mil/hypercube>

<sup>5</sup><http://datamirror.csdb.cn/admin/dataEO1Main.jsp>

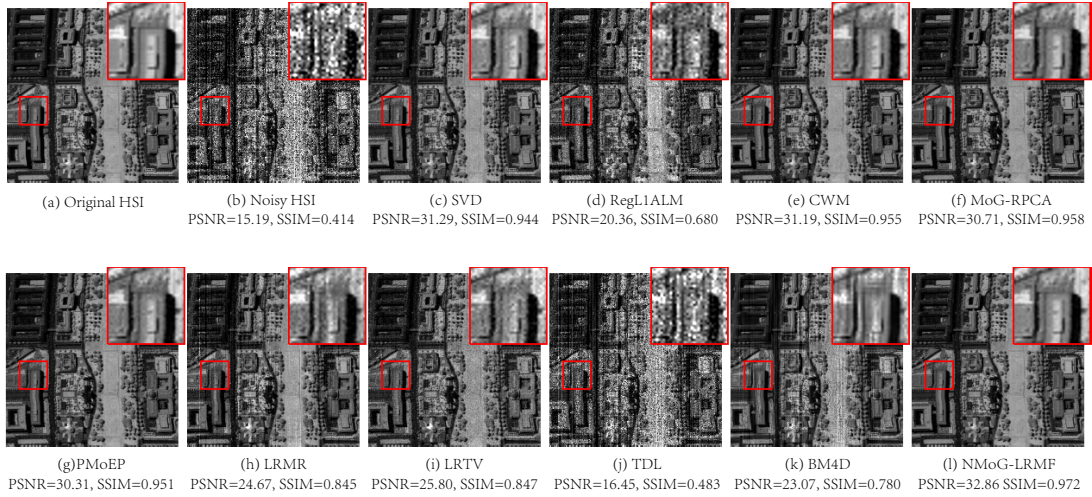


Fig. 5. Restoration results of band 75 under mixture noise in DCsmall data: (a) Original HSI, (b) Noisy HSI, (c) SVD, (d) RegL1ALM, (e) CWM, (f) MoG-RPCA, (g) PMoEP, (h) LRM, (i) LRTV, (j) TDL, (k) BM4D, (l) NMoG. This figure should be better seen by zooming on a computer screen.

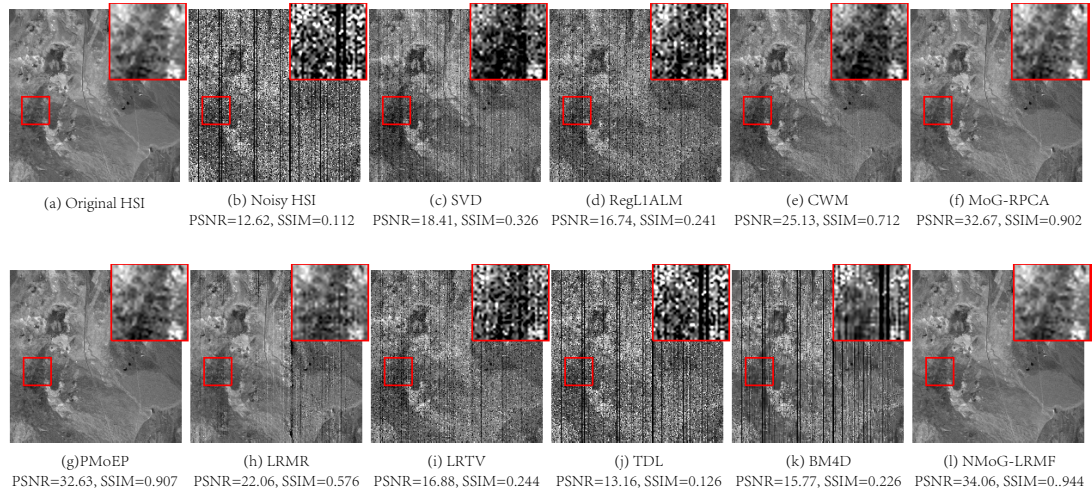


Fig. 6. Restoration results of band 86 under mixture noise in RemoteImage data: (a) Original HSI, (b) Noisy HSI, (c) SVD, (d) RegL1ALM, (e) CWM, (f) MoG-RPCA, (g) PMoEP, (h) LRM, (i) LRTV, (j) TDL, (k) BM4D, (l) NMoG.

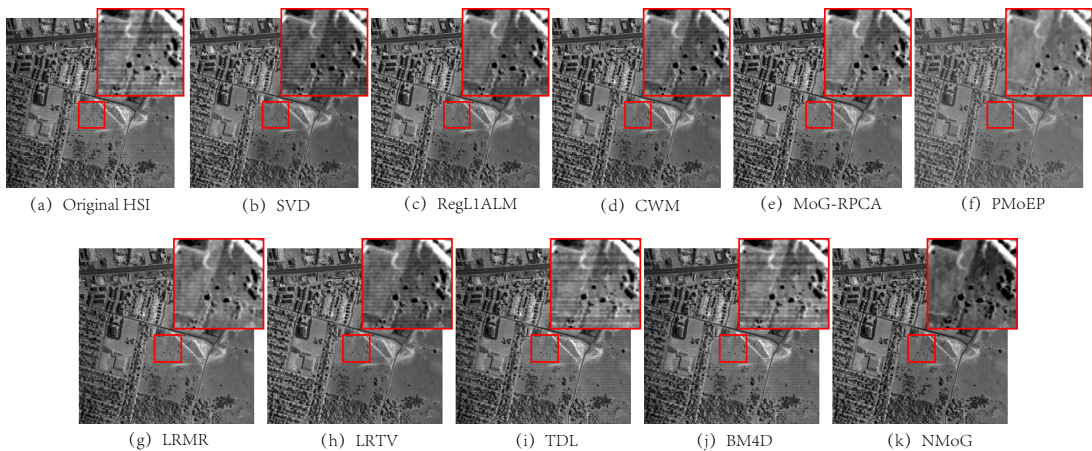


Fig. 7. Restoration results of all methods on band 103 in Urban HSI data. (a) Original HSI, (b) SVD, (c) RegL1ALM, (d) CWM, (e) MoG-RPCA, (f) PMoEP, (g) LRM, (h) LRTV, (i) TDL, (j) BM4D, (k) NMoG.

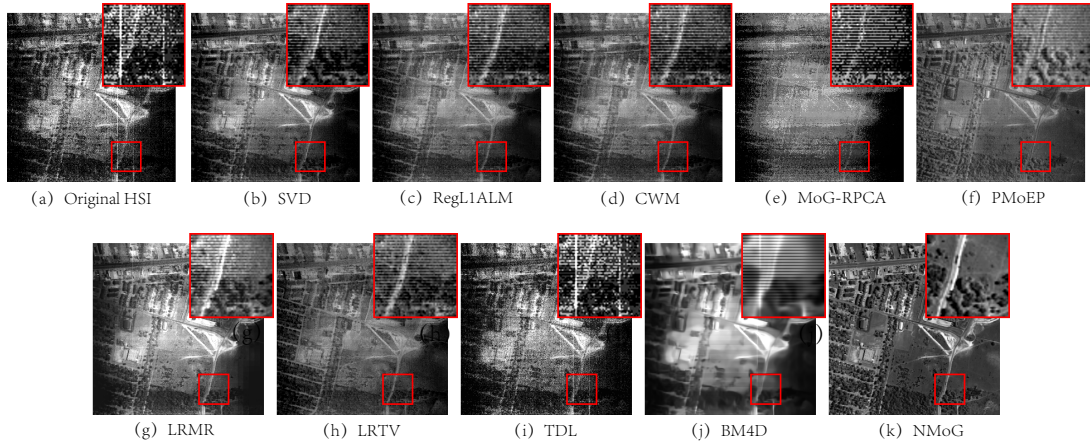


Fig. 8. Restoration results of all methods on band 139 in Urban HSI data. (a) Original HSI, (b) SVD, (c) RegL1ALM, (d) CWM, (e) MoG-RPCA, (f) PMoEP, (g) LRMF, (h) LRTV, (i) TDL, (j) BM4D, (k) NMoG.

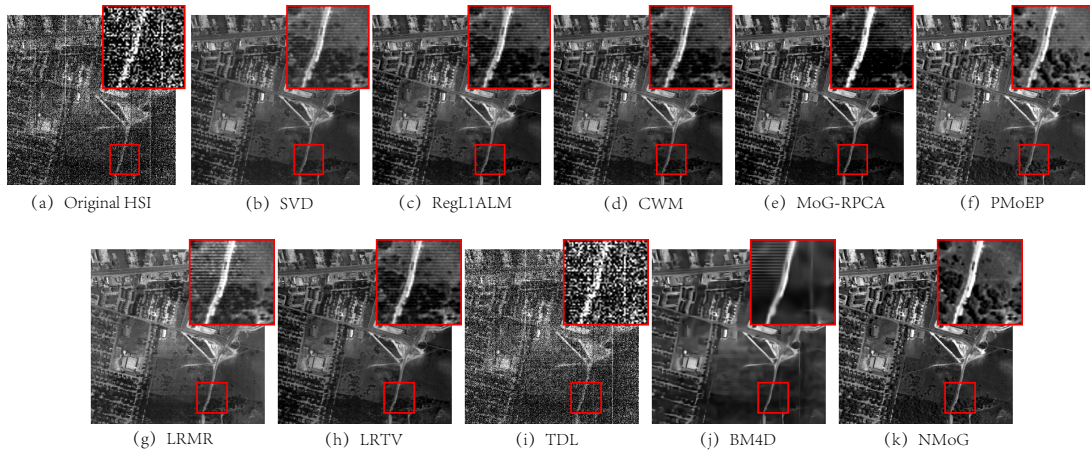


Fig. 9. Restoration results of all methods on band 207 in Urban HSI data. (a) Original HSI, (b) SVD, (c) RegL1ALM, (d) CWM, (e) MoG-RPCA, (f) PMoEP, (g) LRMF, (h) LRTV, (i) TDL, (j) BM4D, (k) NMoG.

rationally verify the robustness of the proposed method in the presence of such heavy noises.

Figs. 7, 8 and 9 present bands 103, 139 and 207 of the restored images obtained by all competing methods, respectively. From Fig. 7-9 (a), we can see that the original HSI bands are contaminated by complex structural noise, like the stripe noise. It can be easily observed from Fig. 7-9 (b)-(f) that the LRMF methods with different i.i.d. noise distribution assumptions cannot finely restore a clean HSI. This can be easily explained by the fact that such structural noises is obvious non-i.i.d. and the deviation between the real noise configuration and the encoded knowledge in the model then naturally degenerate the performance of the corresponding methods. Comparatively, albeit considering less prior knowledge on the to-be-recovered HSI, our method can still achieve a better recovery effect in visualization in its better restoration of texture and edge details and less preservation of structural noises due to its powerful noise modeling ability. This further substantiates the robustness of the proposed method in practical scenarios.

Then we give some quantitative comparison by showing the horizontal mean profiles of band 207 in Urban dataset before and after restoration in Fig. 10. The horizontal axis in the figure represents the row number, and the vertical axis

represents the mean digital number value of each row. As shown in Fig. 10(a), due to the existence of mixed noise, there are rapid fluctuations in the curve. After the restoration processing, the fluctuations are more or less suppressed. It is easy to observe that the restoration curve of our NMoG-LRMF method provides evidently smoother curves.

The second Hyperion dataset is of the size  $3128 \times 256 \times 242$  and some bands are so seriously polluted that all signatures of pixel is equal 0. Thus we only use a subset of its 198 bands in this experiment after removing those zero signatures bands 1-7, 58-76, and 224-242, which are evidently outliers without any intrinsically useful information. We further spatially cropped a square area from the HSI with size  $256 \times 256 \times 198$  with relatively evident noises to specifically testify the denoising capability of a utilized method.

Figs. 11, 12 and 13 show bands 100, 144 and 197 of the restored HSI images by all competing methods. From the figures, it can be easily observed that SVD and TDL methods have little effects in removing the noise; RegL1ALM and CWM methods can only partially eliminate the noise and MoG-RPCA and PMoEP methods have a better performance than SVD, RegL1ALM and CWM due to their better noise fitting ability brought by the MoG and MoEP models. They,

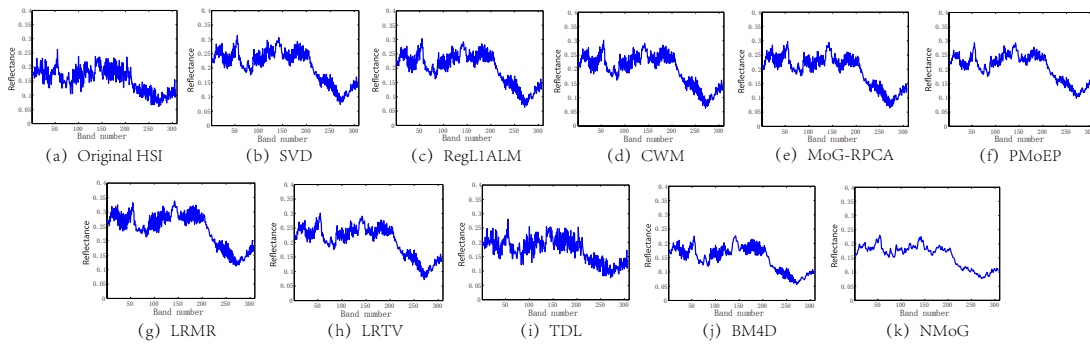


Fig. 10. Horizontal mean profiles of band 207 in Urban HSI data. (a) Original HSI, (b) SVD, (c) RegL1ALM, (d) CWM, (e) MoG-RPCA, (f) PMoEP, (g) LRMR, (h) LRTV, (i) TDL, (j) BM4D, (k) NMoG.

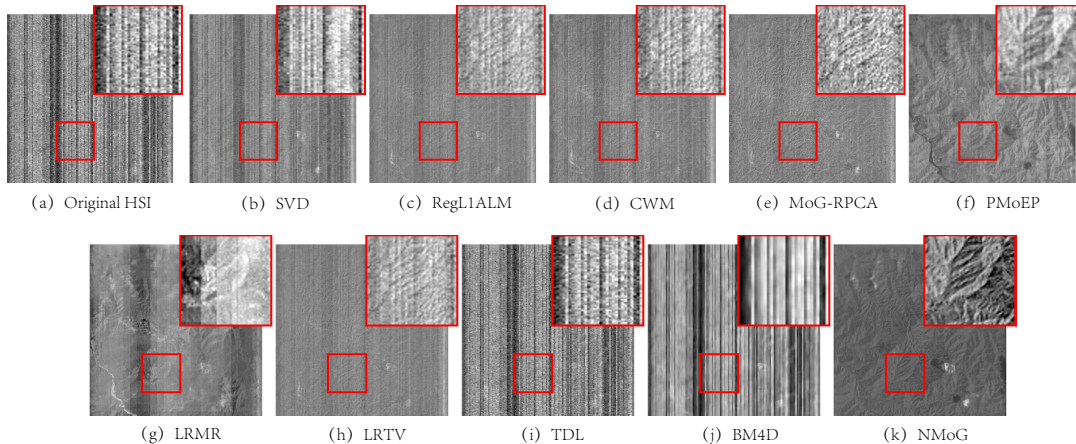


Fig. 11. Restoration results of all methods on band 100 in EO-1 Hyperion data. (a) Original HSI, (b) SVD, (c) RegL1ALM, (d) CWM, (e) MoG-RPCA, (f) PMoEP, (g) LRMR, (h) LRTV, (i) TDL, (j) BM4D, (k) NMoG.

however, still miss lots of details in their HSI recovery due to their implicit improper i.i.d. assumptions on noise distributions under HSI. All other competing methods also cannot achieve a satisfactory HSI denoising results even though they have considered more HSI prior knowledge in their models. Comparatively, the superiority of the proposed method can be easily observed in both detail preservation and noise removing.

Fig. 14 shows the vertical mean profiles of band 100 before and after restoration. As shown in Fig. 14 (a), due to the existence of mixed noise especially the stripes disorderly located in the image, there are evident fluctuations over various places of the curve. After the restoration processing, all competing methods show evident non-smoothness over the corresponding curves, except that obtained from the proposed one. This implies that the HSI obtained by proposed NMoG-LRMF method can better preserve such prior knowledge possessed by real HSIs, as also substantiated by Fig. 10.

### C. Effect of component number on denoising performance

In this section, we examine the sensitivity of NMoG-LRMF method to the setting of the Gaussian component number  $K$ . We run NMoG-LRMF with 20 initializations on the DC Mall data in Gaussian + impluse noise and mixture noise cases, respectively, with  $K$  varying from 1 to 10. The results are shown in Fig. 15. It can be easily observed that after  $K$  is larger than 2, the denoising performance of the proposed

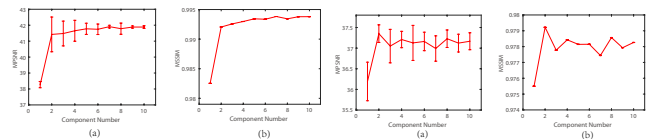


Fig. 15. Stability test of the proposed method to Gaussian component number  $K$  on DC Mall data in Gaussian + impluse noise and mixture noise cases. (a) MPSNR tendency curve with respect to  $K$ . (b) MSSIM tendency curve with respect to  $K$ .

method tends to be stable and not very sensitive to the choice of  $K$  value. Actually, in all our real experiments, we just simply set  $K$  as 3, and our method can consistently perform well throughout all our experiments.

## IV. CONCLUSION

In this paper, we initially propose a strategy to model the HSI noise using a non-i.i.d. noise assumption. Then we embed such noise modeling strategy into the low-rank matrix factorization (LRMF) model and propose a non-i.i.d LRMF model under the Bayesian framework. A variational Bayes algorithm is presented to infer the posterior of the proposed model. Compared with the current state-of-the-arts techniques, the proposed method performs more robust due to its capability of adapting to various noise shapes encountered in applications, which is substantiated by our experiments implemented on synthetic and real noisy HSIs.

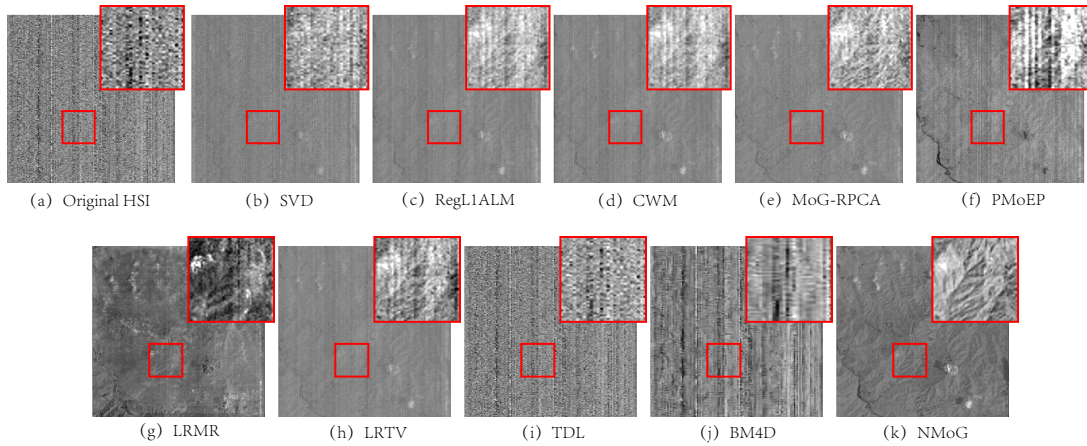


Fig. 12. Restoration results of all methods on band 144 in EO-1 Hyperion data. (a) Original HSI, (b) SVD, (c) RegL1ALM, (d) CWM, (e) MoG-RPCA, (f) PMoEP, (g) LRM, (h) LRTV, (i) TDL, (j) BM4D, (k) NMoG.

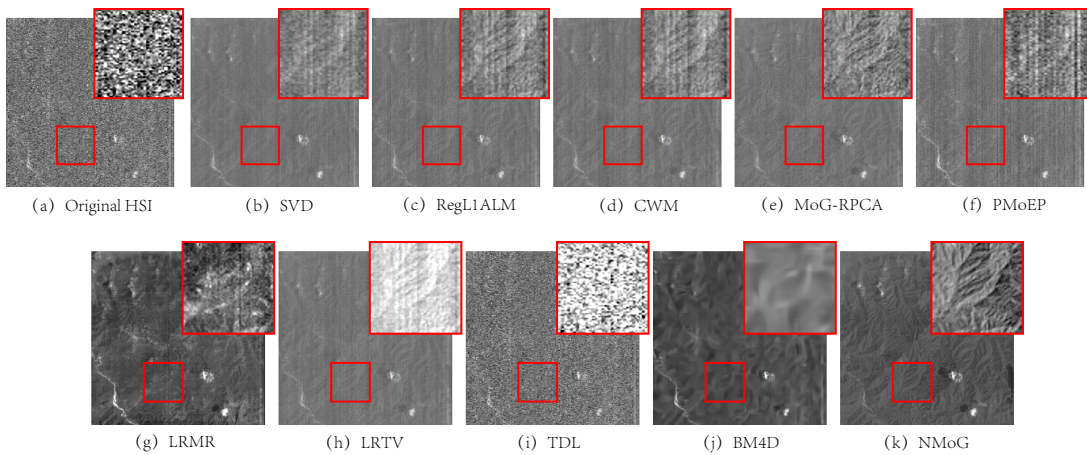


Fig. 13. Restoration results of all methods on band 197 in EO-1 Hyperion data. (a) Original HSI, (b) SVD, (c) RegL1ALM, (d) CWM, (e) MoG-RPCA, (f) PMoEP, (g) LRM, (h) LRTV, (i) TDL, (j) BM4D, (k) NMoG.

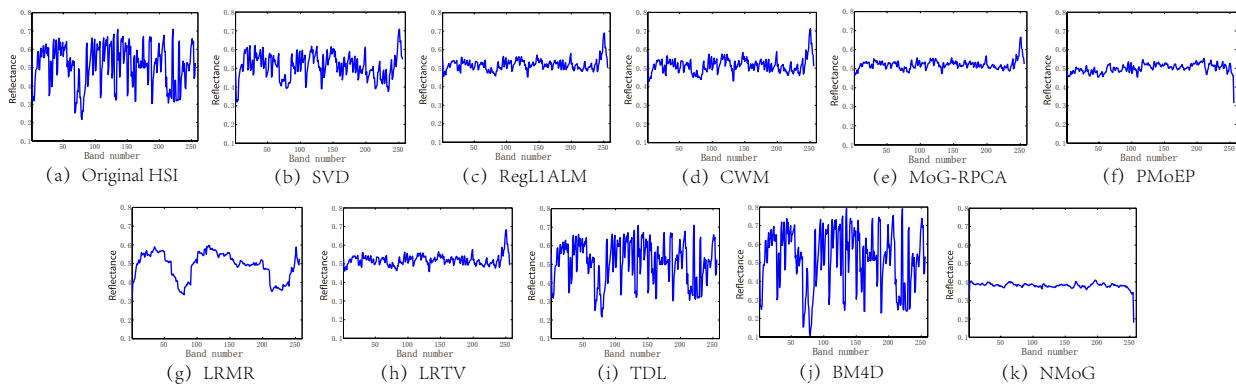


Fig. 14. Vertical mean profiles of band 100 in EO-1 Hyperion data. (a) Original HSI, (b) SVD, (c) RegL1ALM, (d) CWM, (e) MoG-RPCA, (f) PMoEP, (g) LRM, (h) LRTV, (i) TDL, (j) BM4D, (k) NMoG.

In our future work, we will try to extend the application of our method to video and face image data. Also, we will integrate more useful HSI prior terms into our model to further enhance its denoising capability. Besides, the proposed noise modeling strategy can be specifically re-designed under certain application context, like the wind speed prediction problem as indicated in [22], [23].

## REFERENCES

- [1] S. D. Babacan, M. Luessi, R. Molina, and A. K. Katsaggelos. Sparse bayesian methods for low-rank matrix estimation. *IEEE Transactions on Signal Processing*, 60(8):3964–3977, 2012.
- [2] J. M. Bioucas-Dias, A. Plaza, N. Dobigeon, M. Parente, Q. Du, P. Gader, and J. Chanussot. Hyperspectral unmixing overview: Geometrical, statistical, and sparse regression-based approaches. *IEEE Transactions on Selected Topics in Applied Earth Observations and Remote Sensing*, 5(2):354–379, 2012.
- [3] C. M. Bishop. *Pattern recognition and machine learning*. Springer, 2006.
- [4] X. Cao, Y. Chen, Q. Zhao, D. Meng, Y. Wang, D. Wang, and Z. Xu. Low-rank matrix factorization under general mixture noise distributions. In *Proceedings of the IEEE International Conference on Computer Vision*, pages 1493–1501, 2015.
- [5] G. Chen and S.-E. Qian. Simultaneous dimensionality reduction and denoising of hyperspectral imagery using bivariate wavelet shrinking and principal component analysis. *Canadian Journal of Remote Sensing*, 34(5):447–454, 2008.
- [6] G. Chen and S.-E. Qian. Denoising of hyperspectral imagery using principal component analysis and wavelet shrinkage. *IEEE Transactions on Geoscience and Remote Sensing*, 49(3):973–980, 2011.
- [7] G. Chen and W.-P. Zhu. Signal denoising using neighbouring dual-tree complex wavelet coefficients. *IEEE Transactions on Signal Processing*, 6(2):143–147, 2012.
- [8] P. Chen, N. Wang, N. L. Zhang, and D.-Y. Yeung. Bayesian adaptive matrix factorization with automatic model selection. In *Proceedings of the IEEE Conference on Computer Vision and Pattern Recognition*, 2015.
- [9] S.-L. Chen, X.-Y. Hu, and S.-L. Peng. Hyperspectral imagery denoising using a spatial-spectral domain mixing prior. *Computer Science and Technology*, 27(4):851–861, 2012.
- [10] Y. Chen, N. M. Nasrabadi, and T. D. Tran. Hyperspectral image classification using dictionary-based sparse representation. *IEEE Transactions on Geoscience and Remote Sensing*, 49(10):3973–3985, 2011.
- [11] K. Dabov, A. Foi, and K. Egiazarian. Video denoising by sparse 3d transform-domain collaborative filtering. In *Proceedings of the IEEE Conference on Signal Processing*, pages 145–149. IEEE, 2007.
- [12] K. Dabov, A. Foi, V. Katkovnik, and K. Egiazarian. Image denoising by sparse 3-d transform-domain collaborative filtering. *IEEE Transactions on Image Processing*, 16(8):2080–2095, 2007.
- [13] C. Ding, D. Zhou, X. He, and H. Zha. R 1-pca: rotational invariant l 1-norm principal component analysis for robust subspace factorization. In *Proceedings of the 23rd International Conference on Machine Learning*, pages 281–288. ACM, 2006.
- [14] M. Elad and M. Aharon. Image denoising via sparse and redundant representations over learned dictionaries. *IEEE Transactions on Image Processing*, 15(12):3736–3745, 2006.
- [15] A. Eriksson and A. Van Den Hengel. Efficient computation of robust low-rank 1-pca: rotational invariant l 1-norm principal component analysis for robust subspace factorization and matrix approximations in the presence of missing data using the l 1 norm. In *Proceedings of the IEEE Conference on Computer Vision and Pattern Recognition*, pages 771–778. IEEE, 2010.
- [16] A. F. Goetz. Three decades of hyperspectral remote sensing of the earth: A personal view. *Remote Sensing of Environment*, 113:S5–S16, 2009.
- [17] A. A. Green, M. Berman, P. Switzer, and M. D. Craig. A transformation for ordering multispectral data in terms of image quality with implications for noise removal. *IEEE Transactions on Geoscience and Remote Sensing*, 26(1):65–74, 1988.
- [18] M. Haardt and P. Strobach. Method for high-resolution spectral analysis in multi channel observations using a singular value decomposition (svd) matrix technique, Oct. 1 1996. US Patent 5,560,367.
- [19] W. He, H. Zhang, L. Zhang, and H. Shen. Hyperspectral image denoising via noise-adjusted iterative low-rank matrix approximation. *IEEE Transactions on Selected Topics in Applied Earth Observations and Remote Sensing*, 8(6):3050–3061, 2015.
- [20] W. He, H. Zhang, L. Zhang, and H. Shen. Total-variation-regularized low-rank matrix factorization for hyperspectral image restoration. *IEEE Transactions on Geoscience and Remote Sensing*, 54(1):178–188, 2016.
- [21] W. He, H. Zhang, L. Zhang, and H. Shen. Total-variation-regularized low-rank matrix factorization for hyperspectral image restoration. *IEEE Transactions on Geoscience and Remote Sensing*, 54(1):178–188, 2016.
- [22] Q. Hu, Y. Wang, Z. Xie, P. Zhu, and D. Yu. On estimating uncertainty of wind energy with mixture of distributions. *Energy*, 112:935–962, 2016.
- [23] Q. Hu, S. Zhang, Z. Xie, J. Mi, and J. Wan. Noise model based  $\nu$ -support vector regression with its application to short-term wind speed forecasting. *Neural Networks*, 57:1–11, 2014.
- [24] Q. Huynh-Thu and M. Ghanbari. Scope of validity of psnr in image/video quality assessment. *Electronics letters*, 44(13):800–801, 2008.
- [25] H. Ji, C. Liu, Z. Shen, and Y. Xu. Robust video denoising using low rank matrix completion. In *Proceedings of the IEEE Conference on Computer Vision and Pattern Recognition*, pages 1791–1798. IEEE, 2010.
- [26] A. Karami, M. Yazdi, and A. Z. Asli. Noise reduction of hyperspectral images using kernel non-negative Tucker decomposition. *IEEE Transactions on Journal of Selected Topics in Signal Processing*, 5(3):487–493, 2011.
- [27] Q. Ke and T. Kanade. Robust l 1 norm factorization in the presence of outliers and missing data by alternative convex programming. In *Proceedings of the IEEE Conference on Computer Vision and Pattern Recognition*, volume 1, pages 739–746. IEEE, 2005.
- [28] D. Létexier and S. Bourennane. Noise removal from hyperspectral images by multidimensional filtering. *IEEE Transactions on Geoscience and Remote Sensing*, 46(7):2061–2069, 2008.
- [29] J. Liu, P. Musialski, P. Wonka, and J. Ye. Tensor completion for estimating missing values in visual data. *IEEE Transactions on Pattern Analysis and Machine Intelligence*, 35(1):208–220, 2013.
- [30] L. Liu, L. Chen, C. P. Chen, Y. Y. Tang, and C. M. Pun. Weighted joint sparse representation for removing mixed noise in image. 2016.
- [31] X. Liu, S. Bourennane, and C. Fossati. Denoising of hyperspectral images using the parafac model and statistical performance analysis. *IEEE Transactions on Geoscience and Remote Sensing*, 50(10):3717–3724, 2012.
- [32] K. E. M. Maggioni, V. Katkovnik and A. Foi. Nonlocal transform-domain iter for volumetric data denoising and reconstruction. *IEEE Transactions on Image Processing*, 22(1):119–133, 2013.
- [33] V. Maz'ya and G. Schmidt. On approximate approximations using gaussian kernels. *IMA Journal of Numerical Analysis*, 16(1):13–29, 1996.
- [34] D. Meng and F. Torre. Robust matrix factorization with unknown noise. In *Proceedings of the IEEE International Conference on Computer Vision*, pages 1337–1344, 2013.
- [35] D. Meng, Z. Xu, L. Zhang, and J. Zhao. A cyclic weighted median method for l1 low-rank matrix factorization with missing entries. In *Proceedings of the Association for the Advance of Artificial Intelligence*, volume 4, page 6, 2013.
- [36] K. Mitra, S. Sheorey, and R. Chellappa. Large-scale matrix factorization with missing data under additional constraints. In *Advances in Neural Information Processing Systems*, pages 1651–1659, 2010.
- [37] T. Okatani, T. Yoshida, and K. Deguchi. Efficient algorithm for low-rank matrix factorization with missing components and performance comparison of latest algorithms. In *Proceedings of the 28th International Conference on Machine Learning*, pages 842–849. IEEE, 2011.
- [38] H. Othman and S.-E. Qian. Noise reduction of hyperspectral imagery using hybrid spatial-spectral derivative-domain wavelet shrinkage. *IEEE Transactions on Geoscience and Remote Sensing*, 44(2):397–408, 2006.
- [39] Y. Peng, D. Meng, Z. Xu, C. Gao, Y. Yang, and B. Zhang. Decomposable nonlocal tensor dictionary learning for multispectral image denoising. In *Proceedings of the IEEE Conference on Computer Vision and Pattern Recognition*, pages 2949–2956, 2014.
- [40] A. Plaza, J. A. Benediktsson, J. W. Boardman, J. Brazile, L. Bruzzone, G. Camps-Valls, J. Chanussot, M. Fauvel, P. Gamba, A. Gualtieri, et al. Recent advances in techniques for hyperspectral image processing. *Remote Sensing of Environment*, 113:S110–S122, 2009.
- [41] Y. Qian, S. Jia, J. Zhou, and A. Robles-Kelly. Hyperspectral unmixing via sparsity-constrained nonnegative matrix factorization. *IEEE Transactions on Geoscience and Remote Sensing*, 49(11):4282–4297, 2011.
- [42] Y. Qian and M. Ye. Hyperspectral imagery restoration using nonlocal spectral-spatial structured sparse representation with noise estimation. *IEEE Transactions on Selected Topics in Applied Earth Observations and Remote Sensing*, 6(2):499–515, 2013.
- [43] P. Sathya and K. Vani. Hyperspectral image classification. *Advances in Natural and Applied Sciences*, 9(6 SE):338–344, 2015.
- [44] L. Shao, R. Yan, X. Li, and Y. Liu. From heuristic optimization to dictionary learning: a review and comprehensive comparison of image

- denoising algorithms. IEEE Transactions on Cybernetics, 44(7):1001–1013, 2014.
- [45] T. Skauli. Sensor noise informed representation of hyperspectral data, with benefits for image storage and processing. Optics Express, 19(14):13031–13046, 2011.
- [46] D. W. Stein, S. G. Beaven, L. E. Hoff, E. M. Winter, A. P. Schaum, and A. D. Stocker. Anomaly detection from hyperspectral imagery. IEEE Transactions on Signal Processing, 19(1):58–69, 2002.
- [47] M. Wang, J. Yu, J.-H. Xue, and W. Sun. Denoising of hyperspectral images using group low-rank representation. IEEE Transactions on Selected Topics in Applied Earth Observations and Remote Sensing, 2016, Accepted.
- [48] Z. Wang, A. C. Bovik, H. R. Sheikh, and E. P. Simoncelli. Image quality assessment: from error visibility to structural similarity. Image Processing, IEEE Transactions on, 13(4):600–612, 2004.
- [49] Y. W. Q. Z. D. M. Xia Chen, Zhi Han and Y. Tang. Robust tensor factorization with unknown noise. In Proceedings of the IEEE Conference on Computer Vision and Pattern Recognition, 2016.
- [50] R. Yan, L. Shao, and Y. Liu. Nonlocal hierarchical dictionary learning using wavelets for image denoising. IEEE Transactions on Image Processing, 22(12):4689–4698, 2013.
- [51] Q. Yuan, L. Zhang, and H. Shen. Hyperspectral image denoising employing a spectral–spatial adaptive total variation model. IEEE Transactions on Geoscience and Remote Sensing, 50(10):3660–3677, 2012.
- [52] P. W. Yuen and M. Richardson. An introduction to hyperspectral imaging and its application for security, surveillance and target acquisition. The Imaging Science Journal, 58(5):241–253, 2010.
- [53] A. C. Zelinski and V. K. Goyal. Denoising hyperspectral imagery and recovering junk bands using wavelets and sparse approximation. In Proceedings of the IEEE International Conference on Geoscience and Remote Sensing Symposium, pages 387–390. IEEE, 2006.
- [54] H. Zhang, W. He, L. Zhang, H. Shen, and Q. Yuan. Hyperspectral image restoration using low-rank matrix recovery. Proceedings of the IEEE Transactions on Geoscience and Remote Sensing, 52(8):4729–4743, 2014.
- [55] Q. Zhao, D. Meng, Z. Xu, W. Zuo, and L. Zhang. Robust principal component analysis with complex noise. In Proceedings of the 31st International Conference on Machine Learning, pages 55–63, 2014.
- [56] Y.-Q. Zhao, P. Gong, and Q. Pan. Object detection by spectropolarimetric imagery fusion. IEEE Transactions on Geoscience and Remote Sensing, 46(10):3337–3345, 2008.
- [57] Y. Zheng, G. Liu, S. Sugimoto, S. Yan, and M. Okutomi. Practical low-rank matrix approximation under robust  $l_1$ -norm. In Proceedings of the IEEE Conference on Computer Vision and Pattern Recognition, pages 1410–1417. IEEE, 2012.
- [58] P. Zhong and R. Wang. Multiple-spectral-band crfs for denoising junk bands of hyperspectral imagery. IEEE Transactions on Geoscience and Remote Sensing, 51(4):2260–2275, 2013.